metals

MDPI

Article

Fatigue Crack Initiation and Propagation Relation of Notched Specimens with Welded Joint Characteristics

Moritz Braun [1,*], Claas Fischer [2], Jörg Baumgartner [3,4], Matthias Hecht [3] and Igor Varfolomeev [5]

[1] Institute of Ship Structural Design and Analysis, Hamburg University of Technology, 21073 Hamburg, Germany
[2] TÜV NORD EnSys GmbH & Co. KG, 22525 Hamburg, Germany; cfischer@tuev-nord.de
[3] Research Group System Reliability, Adaptive Structures Machine Acoustics SAM, Mechanical Engineering Department, Technical University of Darmstadt, 64287 Darmstadt, Germany; joerg.baumgartner@sam.tu-darmstadt.de (J.B.); joerg.baumgartner@lbf.fraunhofer.de (M.H.)
[4] Fraunhofer Institute for Structural Durability and System Reliability, 64289 Darmstadt, Germany
[5] Fraunhofer Institute for Mechanics of Materials, 79108 Freiburg, Germany; igor.varfolomeev@iwm.fraunhofer.de
* Correspondence: moritz.br@tuhh.de; Tel.: +49-40-42878-6091

Abstract: This study focuses on predicting the fatigue life of notched specimens with geometries and microstructure representative of welded joints. It employs 26 series of fatigue tests on welded and non-welded specimens containing notches located in different material zones, including the parent material, weld metal, and heat-affected zone. Overall, 351 test samples made of six structural steels are included in the present evaluation. For each individual specimen, the stress concentration factor, as well as the stress distribution in the notched section, was determined for subsequent fracture mechanics calculation. The latter is employed to estimate the fraction of fatigue life associated with crack propagation, starting from a small surface crack until fracture. It was shown that the total fatigue life can be realistically predicted by means of fracture mechanics calculations, whereas estimates of the fatigue life until macroscopic crack initiation are subject to numerous uncertainties. Furthermore, methods of statistical data analyses are applied to explore correlations between the S–N curves and the notch acuity characterized by the notch radius, opening angle, and the stress concentration factor. In particular, a strong correlation is observed between the notch acuity and the slope of the S–N curves.

Keywords: notch fatigue analysis; finite element analysis; fracture mechanics; stress gradient; notch acuity; S–N curves; statistical methods; artificial notches

check for updates

Citation: Braun, M.; Fischer, C.; Baumgartner, J.; Hecht, M.; Varfolomeev, I. Fatigue Crack Initiation and Propagation Relation of Notched Specimens with Welded Joint Characteristics. *Metals* **2022**, *12*, 615. https://doi.org/10.3390/met12040615

Academic Editor: Francesco Iacoviello

Received: 9 February 2022
Accepted: 28 March 2022
Published: 2 April 2022

Publisher's Note: MDPI stays neutral with regard to jurisdictional claims in published maps and institutional affiliations.

Copyright: © 2022 by the authors. Licensee MDPI, Basel, Switzerland. This article is an open access article distributed under the terms and conditions of the Creative Commons Attribution (CC BY) license (https://creativecommons.org/licenses/by/4.0/).

1. Introduction

The fatigue life of engineering structures is a complex process that can be divided into several phases. Simplifying this process, three superordinate phases—crack initiation, fatigue crack propagation, and unstable crack growth—are typically considered for the design of engineering structures. In fact, these phases are usually assessed individually. The first phase ends when a small crack has nucleated which is of the size of characteristic microstructure dimensions, e.g., grain size [1]. The second phase is defined by steady fatigue crack propagation. Both phases are primarily governed by the magnitude of cyclic loads. Finally, the third phase is described by unstable crack propagation when approaching the load-carrying capacity of a structure or component. While the first two phases govern the majority of service life, the last phase can be neglected in the fatigue life analysis.

Typically, different fatigue assessment methods are applied to estimate the duration of the fatigue crack initiation and propagation phase, e.g., stress-based fatigue concepts for crack initiation or linear elastic fracture mechanics for crack propagation. Even advanced methods that enable a joint estimation of fatigue crack initiation and propagation

behavior—such as the IBESS procedure [2]—rely on a large number of assumptions or require additional tests to define relevant input parameters.

Different methods have been developed and are still being developed for a holistic fatigue life assessment; however, distinguishing the different phases for welded components is a complex procedure and often relies on assumptions, such as transition crack sizes [3,4]. This is exacerbated by the fact that the ratio between the number of cycles to crack initiation and propagation is typically influenced by the magnitude of external loads: the lower the applied loading, the longer the crack initiation portion [1,5]. Hence, this study aims at shedding light on the relationship between fatigue crack initiation and propagation in welded joints using artificially notched specimens with welded joint characteristics. For this purpose, an extensive experimental database is evaluated including 351 welded and non-welded specimens made of constructional steels of various strength levels, containing notches with varying notch tip radius, opening angles, and notch depths, and positioned in different material zones. The effect and significance of different influencing factors on fatigue crack initiation and propagation, as well as on the shape of stress-life (S–N) curves, is assessed both experimentally and numerically. Compared to other investigations in the literature, e.g., [2,3,6–14], this study employs experimental fatigue data obtained on specimens with both well-defined notch geometry and distinct notch location. This allows for precise stress calculations and for distinguishing between crack propagation behavior in different microstructural zones. Furthermore, for a significant number of the reference fatigue tests, fatigue lives associated with short and long crack initiation are reported, and this information is then used for validating the analysis approach. In addition, a large number of the reference tests include specimens in stress-relieved conditions, which allows for separating the effect of welding residual stresses from that of the notch acuity and microstructure. A particular intention of this paper is to introduce a reproducible analysis approach for predicting fatigue lives of welded joints using, where possible, conventional fatigue crack growth tests, correlations between the hardness and strength properties of particular weld zones, and a unique definition of an initial "technical" crack size. Such an approach, described in Section 4.2, is shown to yield a good accuracy with a rather moderate computational effort and a limited amount of material data required.

This paper, which is an extension of an earlier study [15], is organized as follows. In Section 2, basic relations are introduced which are used further for the analysis of fatigue crack initiation and propagation with a focus on welded joints. Section 3 describes the test series and specimens involved in the present analysis, test procedures, and details of the crack detection in some of the test specimens. Analysis methods applied for evaluating the test results, including finite element and fatigue crack growth calculations, are described in Section 4. A comparison of fatigue lives obtained experimentally and predicted by the analysis, as well as their statistical evaluation, are given in Section 5. Finally, the main findings of this study are discussed in Section 6.

2. Remarks on Fatigue Life Assessment of Welded Joints

Welded joints generally contain fabrication-induced notches that reduce fatigue strength regardless of the presence of other (macro-geometrical) notch effects, as well as imperfections. Typically, the S–N curves for welded joints are steeper than those of base metal, which is related to the notch effect. The respective slope is often fixed to $k = 3$ [16–19], being argued by the fact that the crack initiation phase is short, and the majority of the fatigue life is spent in crack propagation. It can be shown that under simplified conditions, integration of the Paris–Erdogan law ($da/dN = C \cdot \Delta K^m$) leads to an S–N curve with a slope k equal to the exponent m [20].

As mentioned above, a fixed slope $k = 3$ is considered in most rules and recommendations; however, in some documents, shallower slopes of $k = 3.5$ or $k = 4.0$ are recommended for welded details with a low-stress concentration, such as high-quality welds or welds with weld reinforcement removed [21]. Another difference between the major guidelines is the position of the knee point. In some documents, it is set to $N_k = 5 \cdot 10^6$

cycles [18,19] or to $N_k = 10^7$ [16,21], whereas other documents assume a variable position of the knee point depending on the weld details [22,23].

Typically, cracks initiate from one or more locations in weld transitions, such as weld toes, starting from an imperfection or from the point of the highest stress concentration, and retain an approximately semi-elliptical shape during their growth. Since the weld geometry often varies considerably along the weld seam [24], a simplified weld shape is usually considered in assessment procedures. Even though a considerable part of fatigue life relates to crack propagation, welded joints are typically assessed using stress-based concepts [16–18]. The respective design curves already include a variable amount of the crack propagation portion that depends on the specimen shape, in particular, on the notch acuity. In a more general case, the total fatigue life of a welded component until failure, N_f, can be represented by a sequence of the crack initiation and fatigue crack growth (FCG) events, as given by

$$N_f = N_i + N_{FCG} \tag{1}$$

The first term in Equation (1), N_i, is usually estimated using a material S–N curve, an appropriate multi-axial fatigue criterion together with the information on the local stress gradient in the notch root, the highly loaded area and/or material volume, surface roughness, etc. [1,19,25–27]. In the second term, N_{FCG}, can be calculated based on the fracture mechanics methodology [28], while starting from an initial macroscopic surface crack with a size selected according to either the crack detection limit or some simplified rules, see e.g., [29]. Such an initial crack is often considered to have a semi-elliptical shape with a depth of a_0 and the length of $2c_0$. For example, Fiedler et al. [27] define the initial fatigue crack with a surface length ranging between $2c_0 = 0.25$ and 3 mm.

Within the framework of the linear-elastic fracture mechanics, the number of cycles associated with the crack propagation stage can be calculated by numerically integrating an FCG equation of

$$da/dN = f(\Delta K, R_K, C_i) \tag{2}$$

with $\Delta K = K_{max} - K_{min}$ being the stress intensity factor range, $R_K = K_{min}/K_{max}$ the stress intensity ratio, and C_i denoting material parameters derived by fitting to experimental data. The number of such parameters depends on the type of equation selected for the particular application. In particular, for the analysis of the test data presented in Section 3.1, a description of the FCG rates is required, including the stress ratio effect and a proper estimation of the threshold value ΔK_{th}. This is achieved, e.g., by using an FCG equation of the NASGRO type [30].

As the notch stress may exceed the yield strength, the initial surface crack $a_0 \times 2c_0$ can be completely located within the plastically deformed material. Consequently, the applicability of the linear-elastic fracture mechanics and ΔK as the crack driving force parameter becomes questionable. In such a case, a properly defined cyclic J-integral, ΔJ, [31–33] can be employed instead of ΔK to correlate with the fatigue crack growth rates. Engineering estimates of ΔJ [34,35] can be derived based on the reference stress method incorporated in the failure assessment diagram approach [28,36].

3. Experimental Data

3.1. Specimens

For this study, welded joints were manufactured with artificial notches of different notch acuity (different radii and opening angle) to separate the effect of varying notch shape along weld seams from other important influencing factors (loading, geometry, and material characteristics) and to determine the effect of those on fatigue crack initiation and propagation, as well as on the shape of the S–N curves. In addition, well-documented fatigue data on similar specimens from the literature (Fischer et al. [37], Baumgartner [38]) were included in the evaluation, Tables 1 and 2. This is the reason for the range of different specimen geometries.

Table 1. Overview of artificially notched welded specimens.

Steel Type		Opening Angle ω [°]	Notch Radius r [mm]	Notch Depth d [mm]	Stress Concentration Factor K_t [-]	Width in Crack Growth Direction w [mm]	Thickness t [mm]	Number of Notches	Nominal Stress Ratio R	Series Number
S235JR + N	HAZ	0	0.15	3	8.33	9.5	20	1	−1	1
	HAZ	135	0.15	3	5.64	9.5	20	1	−1	2
S355MC	HAZ	15	0.05	5	12.3	8	8	2	0	23
	HAZ	135	0.05	5	6.55	8	8	2	0	22
	HAZ	180	∞[1]	5	~1	8	8	–	0	24
S355J2 + N	HAZ	0	0.15	3	8.33	9.5	20	1	−1	5
	HAZ	135	0.15	3	5.64	9.5	20	1	−1	6
	HAZ	135	0.5	3	3.82	9.5	20	1	−1	7
	WM	135	0.15	3	5.64	9.5	20	1	−1	8
S690QL1	HAZ	0	0.15	3	8.33	9.5	20	1	−1	10
	HAZ	135	0.15	3	5.64	9.5	20	1	−1	11
	WM	160	10	10	1.44	10	15	2	−1	16
	WM	0	0.15	3	8.33	9.5	15	1	−1	17
S960QL	HAZ	15	0.05	5	12.3	8	8	2	0	26
	HAZ	15	0.5	5	4.08	8	8	2	0	25
	HAZ	135	0.05	5	6.55	8	8	2	0	29
	HAZ	135	0.5	5	3.10	8	8	2	0	28
	HAZ	180	∞ [1]	5	~1	8	8	–	0	27

[1] unnotched specimens with a constant cross-section.

Table 2. Overview of base material-type specimens.

Steel Type	Open-ing Angle ω [°]	Notch Radius r [mm]	Notch Depth d [mm]	Stress Concentration Factor K_t [-]	Width in Crack Growth Direction w [mm]	Thickness t [mm]	Number of Notches	Nominal Stress Ratio R	Series Name
S355J2 + N	135	0.15	3	5.64	9.5	20	1	−1	4
	0	0.15	3	8.33	9.5	20	1	−1	13
QStE380TM	15	0.05	5	12.3	8	8	2	0	18
	15	0.5	5	4.08	8	8	2	0	20
	135	0.05	5	6.55	8	8	2	0	19
	135	0.5	5	3.10	8	8	2	0	21
S690QL1	0	0.15	3	8.33	9.5	15	1	−1	15
	160	10	10	1.44	10	15	2	−1	14

The specimens show typical weld characteristics: firstly, they have different sharp notches with a notch opening angle of $0° \leq \omega \leq 15°$ (weld root failure at partial penetration welds), $\omega = 135°$ (weld toe failure at fillet welds), $\omega \geq 160°$ (mild weld toe at the butt joint) and $\omega = 180°$ (butt joints ground flush). Secondly, the notch radius is typically very small but varies strongly depending on the welding process. This fact is considered by using radii down to $r = 0.05$ mm. The majority of specimens were machined from MAG-welded butt joints with the notch placed in the heat-affected zone (HAZ) or the weld metal (WM), Table 1. These specimens were stress relieved by annealing after welding. Additionally, some specimens were investigated from non-welded plates, Table 2, referred to as base metal (BM) specimens. Overall, six different steel grades were considered, ranging from S235 to S960.

Figure 1 shows schematically the specimen geometries employed in this study. These can be divided into two groups: some of the specimens have two symmetrical notches, whereas the others are notched asymmetrically, which assures crack initiation at the specimen side with a sharper notch.

3.2. Specimen Characterisation

To characterize the specimens, measurements of the actual geometry after specimen preparation and of hardness values were performed. The results of the hardness measurements are presented in Figure 2. For the welded joints, measurements were performed either for all relevant zones (BM, HAZ, and WM) and for top, middle and bottom layers (S235JR + N, S355J2 + N, S690QL1) or only for the zones where the crack initiation occurred (S355MC, QStE380, S960QL).

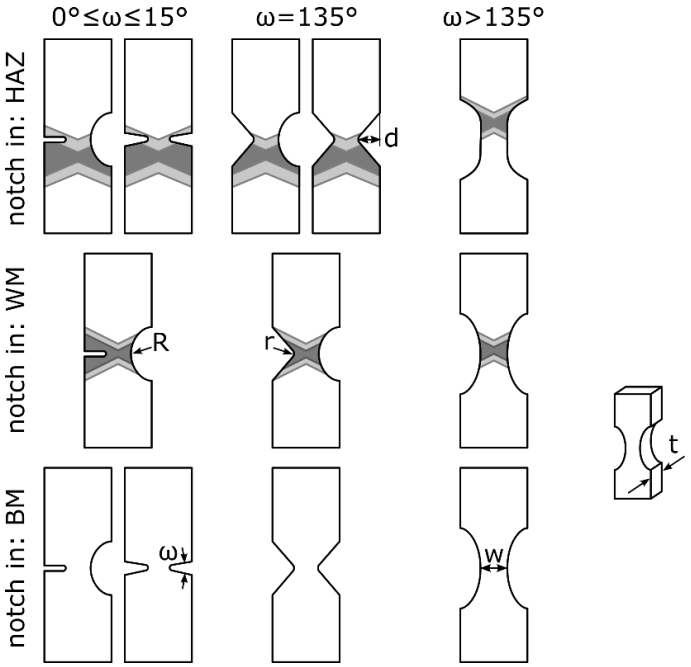

Figure 1. Overview of the specimens used for the evaluation (schematic, not to scale).

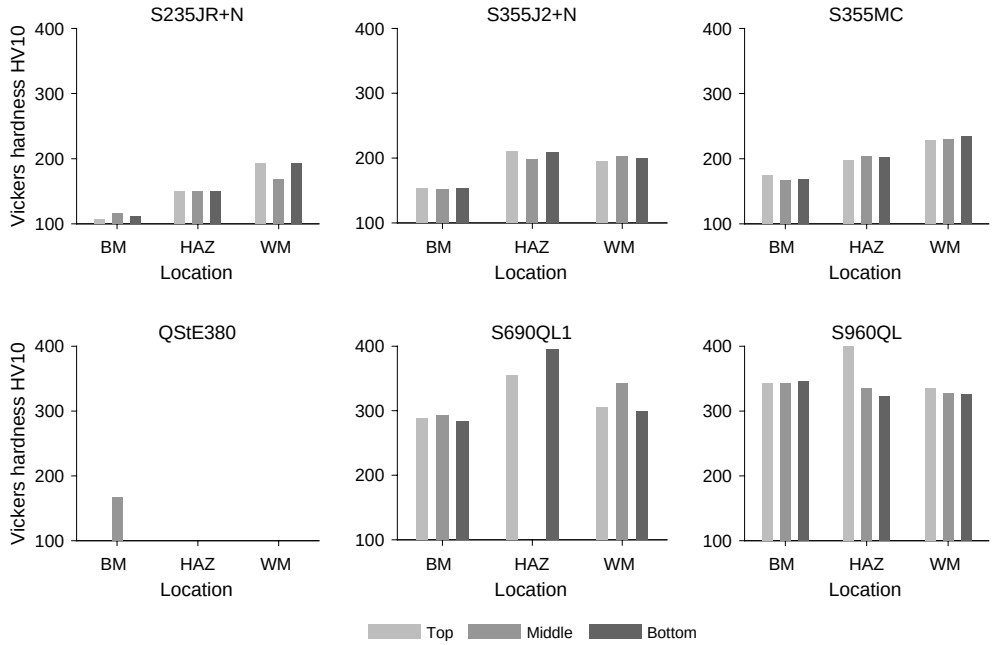

Figure 2. Hardness measurements for the six steel grades with results for the different zones and layers of the welded plates according to ISO 6507-1:2005, data from [39].

3.3. Specimen Preparation

The specimens for test series 1–17 (asymmetric notch geometry) were taken from welded plates with reinforcements removed by grinding. For this, two plate strips were joined by manual metal active gas welding using an X-butt joint with corresponding weld preparation and several alternating weld passes (eight layers for S235 and S355; 14 layers for S690). Most of the plate strips were fixed in a relatively stiff frame during welding in order to reduce the axial misalignment and the induced angular distortion. Afterward, stress annealing was applied to the welded plates.

In the next step, the individual specimens of each series were saw-cut from the butt-welded plates. The specimens were 400 mm long, 20 mm wide, and 15 mm thick.

Then the side surfaces in the direction of the welding were polished and acid-treated to make the HAZ visible with the aim to place the notch tip in a controlled way. Finally, the intended surface notches were produced by wire electro-erosion, resulting in a net thickness $w = 9.5$ mm.

In case of relatively large misalignments on a specimen, its ends were additionally milled over 60 mm in length. Thus, high additional stresses caused by clamping the specimens in the testing machine were avoided.

Furthermore, each individual specimen's geometry and the existing axial and angular misalignments were measured. Because of misaligned specimens, the notch depth d of the rounding and the notch vary amongst specimens, but w is fixed. The individual notch depths were also measured.

The specimens for test series 18–29 were taken from plates with a thickness of $t = 10$ mm. Whereas the plate made from QStE380TM was non-welded, the plates made from S355MC and S960QL were MAG-welded as a butt joint in an X-configuration. Both sides of all plates were ground to reach a final thickness of $t = 8$ mm. The final specimen geometry was extracted from the plates by wire electro-erosion, Figure 3. For test series with notches in the heat-affected zone, the notches were positioned after etching the plate edges.

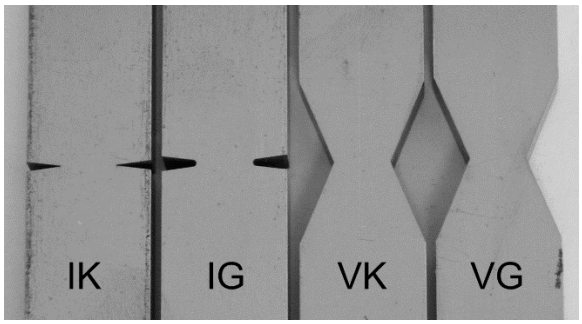

Figure 3. Specimen of test series 18–21.

3.4. Test Procedure

The existing misalignments on specimens of series 1–17 cause additional bending stresses after clamping which interfere with the applied nominal tensile stress. Both stresses are included in the structural stress, which was measured by strain gauge 2 (denoted as "DMS 2" in Figure 4) during a static pre-test for each specimen. The gauge was bonded on the specimen surface at a distance of 160 mm from the end so that the related signal was not affected by the notch. The opposite strain gauge "DMS 3" was applied to a few specimens only to verify the stress distribution over the thickness. Moreover, the strain gauge "DMS 1" was used to detect crack initiation by measuring an altered strain distribution due to the presence of a crack.

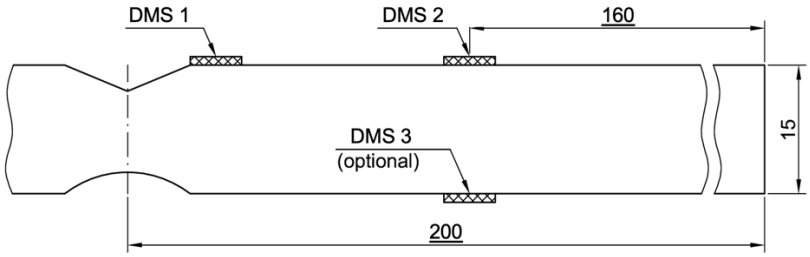

Figure 4. Schematic presentation of the specimen geometry for series 1–17 including the strain gauge positions to detect crack initiation and misalignment-related secondary bending stresses, adapted from [37].

The specimens at the ends that are not milled had different local stress ratio's R_{notch} at the notch, which was caused by the angular misalignments. For the consistency of their evaluation in terms of S–N curves, all test results were adjusted to $R_{notch} = 0$. For this purpose, a mean stress correction $f(R_{notch})$ was applied. For notched specimens with $\omega = 135°$ from Fischer et al. [37], $f(R_{notch})$ was taken from the recommendations of the International Institute of Welding [16] for stress-relieved welded joints. The correction factor used for the sharp notch was experimentally determined by evaluating test results gained under two nominal stress ratios $R = -1$ and $R = 0$. The difference with respect to the mean fatigue strength (survival probability of $P = 50\%$) at $N = 2 \cdot 10^6$ cycles is the mean stress effect, being a factor of 1.67, which is experimentally determined. For the base material specimens, the values of $f(R_{notch})$ were estimated according to the FKM guidelines [19]. Finally, the corrected structural stress ranges were used as the loading condition in the finite element (FE) analyses, aiming to compute the local fatigue parameter at the notch tip (the stress gradient, for instance).

Fatigue testing machines with hydraulic clamps were used in all tests. The tests were performed under a constant force range, at room temperature, at a frequency of about $f = 32$ Hz, on average. The nominal stress ratio was $R = 0$ for test series 1–17 and $R = -1$ for series 18–29. Each test was conducted until the specimen's failure with the related number of cycles denoted by N_f; however, a test was stopped between $N_G = 2 \cdot 10^6$ and $N_G = 1 \cdot 10^7$ cycles when either an initial crack was not visually detected and a decrease in the strain gauge signal, if available, was not noted. Then, the specimen was marked as a run-out and was re-tested to fracture under a larger nominal stress range. In case a crack initiation was detected before N_G cycles, the test was continued until failure.

3.5. Crack Detection

Two methods were applied for crack detection. Crack length foils were bonded to the side surface of specimens of the series 13, 15, and 17. For series 13, the first resistor strand was located approx. 0.5 mm below the notch root. The measures were aimed at originally catching the crack propagation quantitatively. For series 15 and 17, a similar method was used with 0.1 mm spacing between the strands and 0.1 mm distance to the notch root, see Figure 5a. For series 18–29, a digital camera was used for the optical detection of crack initiation and propagation on some of the specimens, see Figure 5b, with a resolution of approx. 150 pixels per mm. Pictures of the notches were taken at isochronous timing. For every test specimen, a minimum of 50 pictures were recorded. In order to improve the resolution of the crack initiation detection, a very small layer of a mixture of zinc oxide and glycerin was applied on the notch surface. With this approach, crack length on the surface down to 0.2 mm could be made visible. For the evaluation of cycles to crack initiation, a crack length of 0.5 mm on the surface was used as the failure criteria.

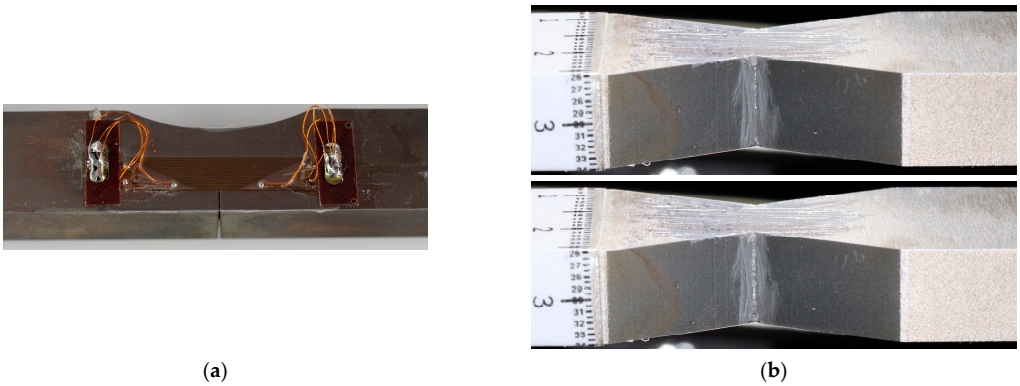

(**a**) (**b**)

Figure 5. (**a**) Specimen with attached crack gauge after removal of weld overfill and wire erosion of notch into the middle of the weld metal and (**b**) two consecutive pictures of crack detection with photographs (specimen from test series 22).

The pictures were evaluated visually. As the first crack initiation criterion, a crack length on the surface of 1.0 mm was chosen as a *small crack initiation*. As soon as the first cracks appeared on the side surface of the specimen, the failure criterion of the *long crack initiation* was assigned. Similarly, crack initiation and propagation were monitored and assigned to the different stages by assessing the changing strain signals of the crack detection gauges, see Figure 6.

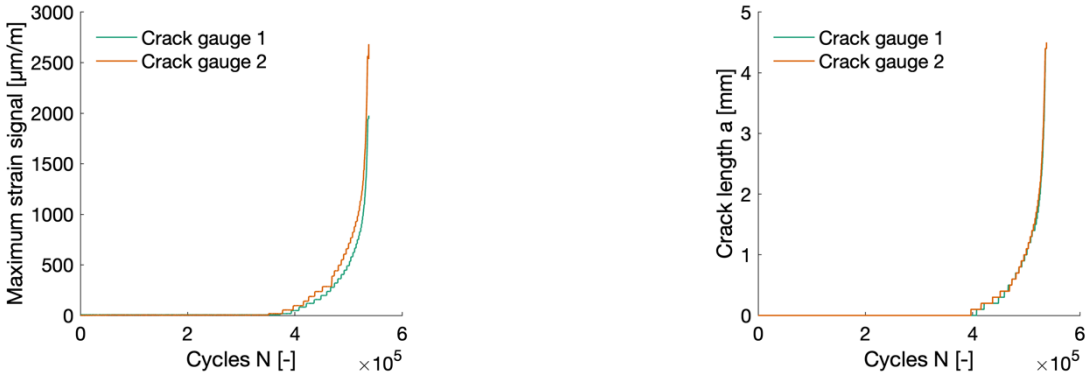

Figure 6. (**a**) Strain signal measurement of two crack gauges at top and bottom side over a number of cycles for a specimen of the series 15; (**b**) Crack lengths derived from strain signals.

3.6. Statistical Evaluation of Fatigue Test Results

In the statistical evaluation, the following parameters of the S–N curves were identified:

- endurable nominal stress at the knee point $\Delta\sigma_{n,k}$,
- number of cycles at the knee point N_k,
- slope of the S–N curve in the high cycle fatigue regime $(N \leq N_k)$,
- slope of the S–N curve in the very high cycle regime $(N > N_k)$.

Since k^* is quite difficult to identify [40], it was set to $k^* = 45$ according to Sonsino [41].

The statistical evaluation of the S–N curve was performed using the maximum likelihood method [40]. A mathematical best fit S–N curve was calculated, Figure 7 (left), by varying the knee point, Figure 7 (right), and identifying the one with the highest probability, i.e., with the smallest value of the support function [42] that is the natural logarithm of the probability. It must be mentioned that this location of the knee point does not necessarily align with the one leading to the smallest standard deviation or the scatter defined as $T_S = \Delta\sigma(P_S = 90\%)/\Delta\sigma(P_S = 10\%)$. The results of the statistical evaluation are the S–N curve parameters for all test series, Table A1.

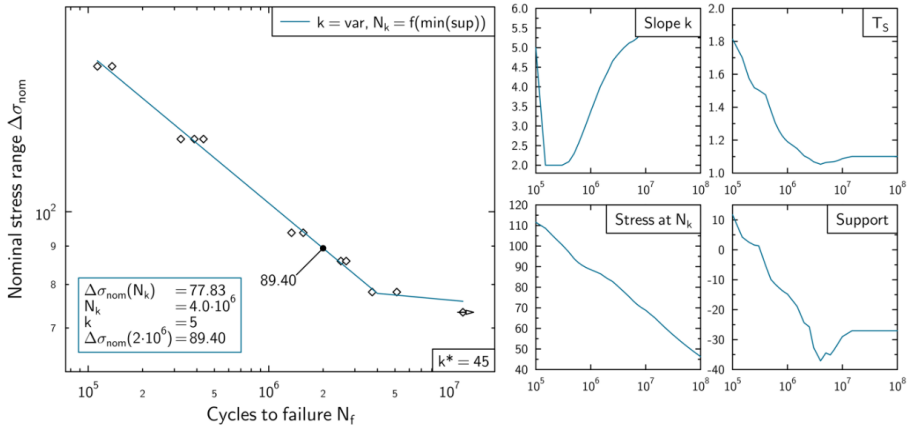

Figure 7. Example of a statistical evaluation of an S–N curve with maximum likelihood (test series 18). Left: Evaluated S-N curve, right: S-N curve parameters in relation to the position of the knee point N_k

4. Calculations

4.1. Stress Calculations

In order to perform the crack initiation or crack propagation assessment, FE models were set up based on the recommendations for mesh refinement for different effective stress methods by Braun et al. [43]. Accordingly, 32 elements per 360° with quadratic shape function are sufficient to accurately determine effective stresses at the notch, see Figure 8. As mentioned in Section 3.4, for the specimens affected by misalignment, the structural stress at strain gauge "DMS 2" consists of membrane stress and bending stresses that are caused either by clamping or tensioning the axially misaligned specimen with milled ends (secondary bending stress), see Fischer et al. [37]; therefore, the structural stress range applied in the FE analyses is equal to the membrane stress because the constant clamping stress vanishes and the secondary bending stress is negligibly small. In the case of milled specimen ends, the clamping stress does not exist, hence, the applied structural stress range results from a superposition of membrane and bending stress.

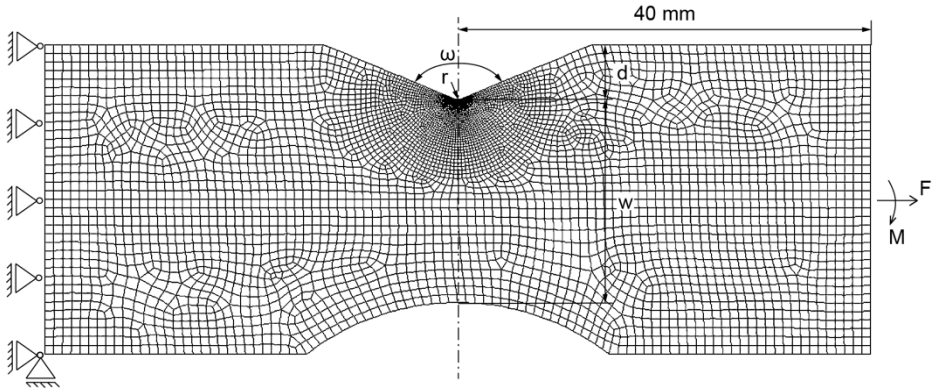

Figure 8. Parametric finite element model of the investigated specimens presented exemplarily for one specimen of series 7.

For each specimen, the stress profiles are then obtained from the location of the first principal stress (at the notch root) and in the crack growth direction. Examples of stress gradients obtained for all specimens of series 6 (S355, $r = 0.15$ mm, $\omega = 135°$, WM) and 1 (S235, $r = 0.15$ mm, $\omega = 0°$, HAZ) are presented in Figure 9. Differences in stress gradients are clearly visible from the comparison, which are due to varying applied nominal stresses as well as different ratios between the membrane and bending stress; however, the normalized gradients are almost identical. Hence, only one line is visible on the right-hand side in Figure 9.

4.2. Fatigue Crack Growth Calculations

To support fracture mechanics calculations, fatigue crack growth data for construction steels were collected describing the FCG rates both in the threshold and in the Paris regime at various stress ratios. Among the results available in the literature, Zerbst [44] provides comprehensive data for the materials S355NL and S960NL, shown as symbols in Figure 10. Note that a considerable number of welded specimens described in Section 3 exhibited misalignment and thus were subjected to superimposed tension and bending loading during fatigue testing (Section 4.1). Consequently, the nominal stress ratio, R, varied from specimen to specimen, while the stress intensity ratio, R_K, additionally varied in the course of crack propagation as a function of the crack depth. To consider this effect, the experimental data [44] were smooth curve fitted by the NASGRO-type function [30], as shown by the curves in Figure 10. These were employed for all specimens of the same material designation, however, without distinguishing between the base material, weld metal, and heat-affected zone. Moreover, since no sufficient data were found for other materials specified in Tables 1 and 2, the following assumptions were made:

- FCG curves for S355NL, Figure 10a, were adopted for S235JR + N, S355MC, S355J2 + N and QStE380TM,
- FCG curves for S960NL, Figure 10b, were adopted for S690QL.

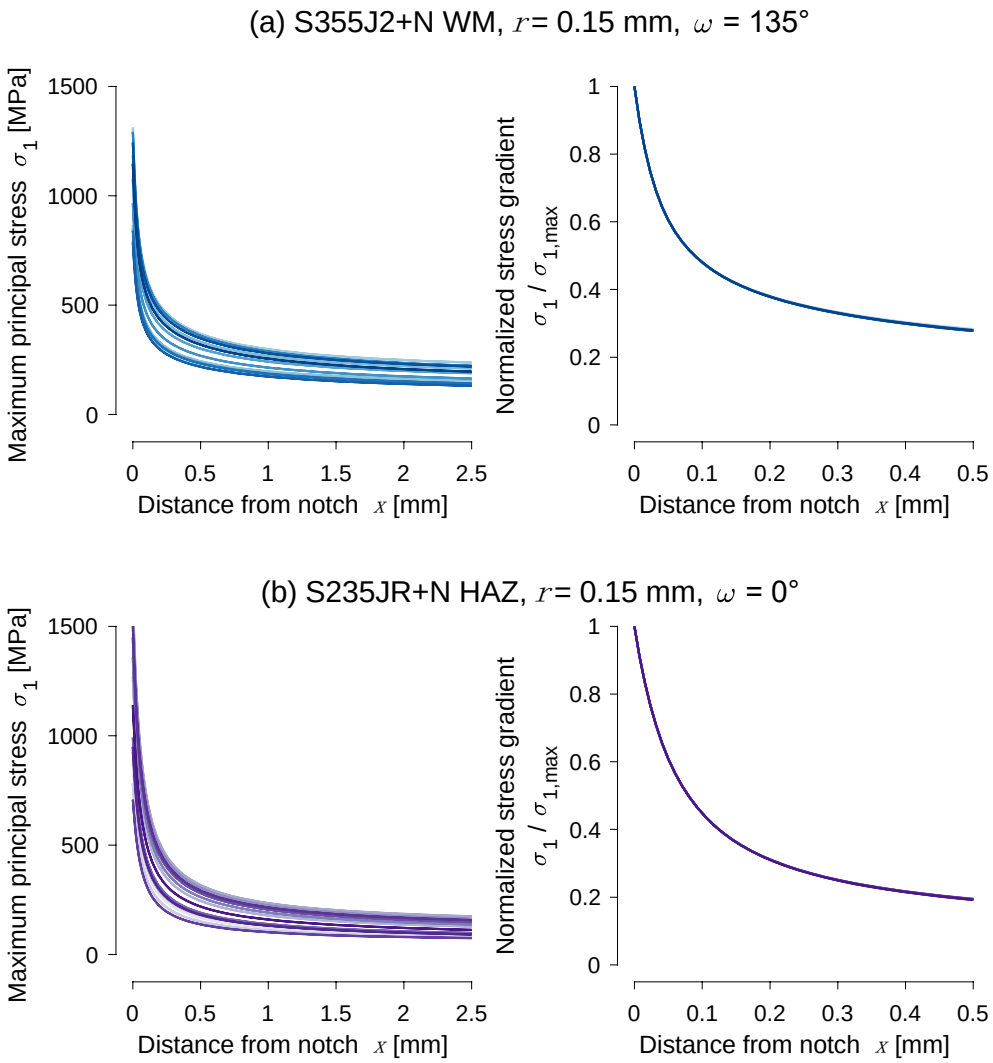

Figure 9. Exemplary stress gradients in crack growth direction of the specimens of series 6 (**a**) and 1 (**b**), as well as corresponding stress gradients normalized with the maximum principal stress at the notch tip.

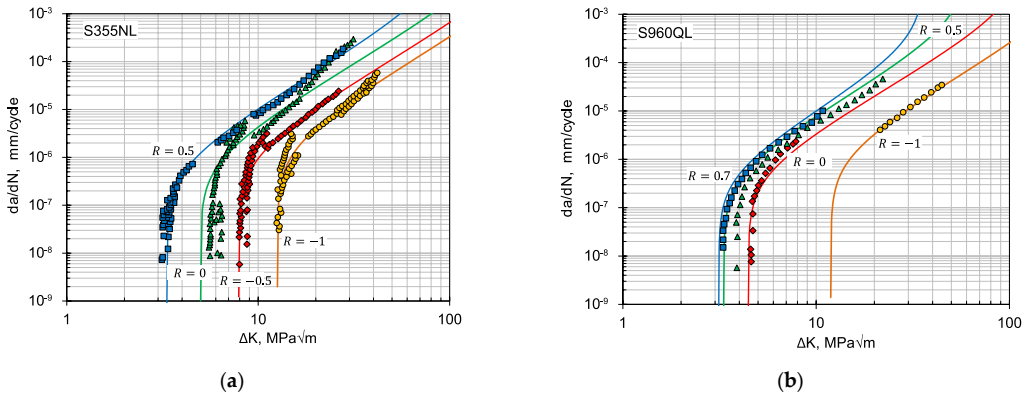

(**a**) (**b**)

Figure 10. FCG curves for S355NL (**a**) and S960QL (**b**). Symbols: experimental data from [44], curves: analytical fit data from [30]. Symbols and curves of the same color correspond to the same R value.

In the fatigue crack growth calculations, an initial semi-circular surface crack was considered to be located in the notch root at the center of the specimen thickness, t. Such a crack, referred to as a short crack (index "sc"), was assumed to have unique dimensions for all test specimens: the crack depth of $a_{sci} = 0.5$ mm, and the crack length of $2c_{sci} = 1$ mm similar to the recommendation by Radaj et al. [1]. Thereafter, two stages of crack propagation were analyzed. The first one corresponds to the growth of the initial short crack until complete penetration through the specimen thickness, ending up at $2c = t$ and $a = a_{lc}$. Here, a_{lc} denotes the depth of a resulting through-thickness, or long crack. Subsequent crack growth, starting at $a = a_{lc}$ until final fracture, corresponds to the second stage of crack propagation. The total fatigue life associated with fatigue crack propagation, N_{FCG} in Equation (1), is then determined by

$$N_{FCG} = N_{sc} + N_{lc} \tag{3}$$

where N_{sc} and N_{lc} are the load cycles associated with the first and the second stages, respectively. Given the total fatigue life, N_f, and provided the quantities on the right-hand side of Equation (3) can be estimated by fracture mechanics calculations, the number of load cycles until short crack and long crack initiation can be deduced from

$$N_{sci} = N_f - N_{sc} - N_{lc} \tag{4}$$

and

$$N_{lci} = N_f - N_{lc} \tag{5}$$

respectively.

High-stress concentration factors (maximum elastic stress at the notch root divided by the nominal stress, see Section 4.1), reported in Tables 1 and 2, suggest that a significant amount of the tested specimens revealed plastic deformations in the notch root at a potential crack initiation location. As mentioned in Section 2, the linear-elastic fracture mechanics methods need to be modified in such a case to account for material yielding. For this purpose, an analytical approach is adopted in the present study, as described below.

Given the upper and the lower stress intensity factors in a load cycle, K_{max} and K_{min}, their plasticity corrected values are calculated based on the FAD methodology:

$$K_{J,max} = \frac{K_{max}}{f(L_{r,max})},\ K_{J,min} = \frac{K_{min}}{f(L_{r,min})}\ . \tag{6}$$

Here, $f(L_r)$ is the failure line according to [36], and L_r the plasticity parameter determined from the reference stress or, alternatively, from the plastic limit load for a particular crack configuration. Thereby, the plasticity correction applies only to an open crack: in the case of $K_{min} \leq 0$ or $K_{min} \leq K_{max} \leq 0$, the denominator in Equation (6) is set to $f(L_r) = 1$. Accordingly, the following two parameters

$$\Delta K_J = K_{J,max} - K_{J,min},\ R_{K_J} = \frac{K_{J,min}}{K_{J,max}}\ . \tag{7}$$

substitute the ΔK and R_K values in the fatigue crack growth equation.

Note that this definition of an "effective" stress intensity factor range, ΔK_J, differs from those suggested in [34] or [35]. First, it does not involve a crack closure term for which the estimate is rather ambiguous. Second, it seems that using the whole range ΔL_r instead of L_r in Equation (6) may lead to an overestimation of the crack driving force at $R_K < 0$ and vice versa at $R_K > 0$. Note also that no residual stresses were considered in the analyses since most of the welded specimens were stress annealed after their manufacturing.

When calculating the first FCG stage, N_{sc} or short crack growth, the stress intensity factor and the parameter L_r were evaluated using the corresponding solutions for a plate with a semi-elliptical surface crack according to [45,46]. In the second FCG stage, N_{lc} or long crack growth was analyzed based on the model of an extended surface crack of a constant depth, and respective K and L_r solutions from [47,48].

The calculations of the function $f(L_r)$ require the knowledge of the material yield strength, $R_{p0.2}$, and the ultimate strength, R_m. Those properties were not available for all the material zones and steel grades considered. Therefore, and for the sake of consistency, the strength properties were estimated in all cases based on correlations with the hardness HV [49]:

$$R_{p0.2} = -90.7 + 2.876HV, \quad R_m = -99.8 + 3.734HV \tag{8}$$

The results of the hardness measurements are summarized in Figure 2.

5. Results

5.1. Assessment of Fatigue Test Results

To be able to assess the accuracy of the fatigue crack growth calculations, the effects on the measured crack initiation and propagation behavior were first assessed. Typically, the ratio between the number of cycles until crack initiation and fracture is influenced by the magnitude of the applied loading, see Radaj et al. [1] and Murakami [5]. As specimens with a wide range of stress concentration factors K_t were tested, the ratio between experimental cycles to short $N_{sci,exp}$ and long crack initiation $N_{lci,exp}$ to the cycles to fracture $N_{f,exp}$ are plotted over the applied notch stress range $\Delta\sigma_{notch}$ in Figure 11. The latter is defined as the product of nominal stress $\Delta\sigma_{nom}$ and stress concentration factor K_t. All results are corrected to $R_{\text{notch}} = 0$ with the aforementioned mean stress correction functions $f(R_n)$.

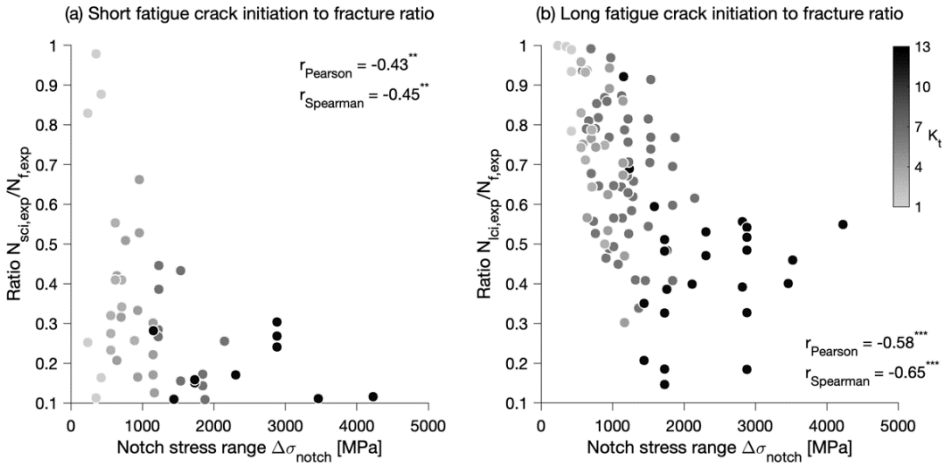

Figure 11. Comparison of ratios between (**a**) cycles until short or (**b**) long crack initiation with cycles to fracture (notch stress range mean stress corrected to $R_{\text{notch}} = 0$).

Two different types of correlation coefficients are determined to assess the statistical interference between the applied notch stress range $\Delta\sigma_{notch}$ and the ratios $N_{sci,exp}/N_{f,exp}$ and $N_{lci,exp}/N_{f,exp}$. The first one is the Pearson correlation coefficient, which determines a linear correlation between two variables based on their covariance, divided by the product of their standard deviations. The second one is Spearman's rank correlation, which assesses whether there is a monotonic relation between both input parameters. Hence, it is also capable of assessing non-linear relations. Pearson's correlation coefficient is not suitable for such relations. This is an important aspect, as the relation between the number of cycles to failure and the applied loading follows a power law (Basquin's equation). This effect is expected to be accounted for more effectively by Spearman's rank correlation than by Pearson's correlation.

In addition, Spearman's rank correlation is relatively robust against outliers [50]. Definitions of moderate to strong correlations vary in the literature; however, values above $|r_{xy}| = 0.7$ are often associated with strong correlation and values below $|r_{xy}| = 0.3$ are typically considered weak.

From Figure 11a, moderate Pearson's and Spearman's type correlations between the ratio $N_{sci,exp}/N_{f,exp}$ are observed. In contrast, an almost strong correlation is determined between the ratio $N_{lci,exp}/N_{f,exp}$ in Figure 11b. This effect is thought to be related to two aspects. First, there is more data available for long crack initiation $N_{lci,exp}$, as the crack detection gauges cannot detect a semi-elliptical surface crack on the surface of the notch, and second, it is more difficult to determine a small semi-elliptical crack reliably. This can also be seen by the larger scatter of results for small to moderate notch stress ranges $\Delta\sigma_{notch} < 500$ MPa in Figure 11a—ranging from almost immediate crack initiation to crack initiation just before final fracture.

In summary, the results agree with the general understanding that the crack initiation portion dominates in the high-cycle fatigue regime whereas, for crack propagation in the medium- and low-cycle fatigue regime, see Radaj et al. [1].

5.2. Comparison of Fatigue Test Results and Fatigue Life Estimates Based on FCG Calculations

Figure 12a is a plot of fatigue lives for the notched specimens measured experimentally, $N_{f,exp}$, and those predicted by fracture mechanics calculations, $N_{FCG,pre}$. The latter does not include the load cycles N_{sci} required for short crack initiation and, thus, tend to underestimate the total fatigue life. Indeed, for 77% of all data, the calculated points are allocated below the 1:1 line in the diagram. At the same time, almost all data are located within a threefold scatter band bound by the 1:3 and 3:1 lines. An exception is mainly for the tests classified as runouts (no crack initiation), while an initial crack was inevitably assumed in the fracture mechanics calculations. Another exceptional point is located above the 1:3 line, in the area of non-conservative prediction, and relates to an S690QL HAZ sample with the notch characteristics $\omega = 135°$, $R = 0.15$ mm, and $K_t = 5.64$ (test series 11). This outlier can be explained by (i) uncertainties in the material data assumed for S690QL and its HAZ, and (ii) the fact that the respective sample was tested at a stress level considerably exceeding the yield strength. As a consequence, that sample revealed the shortest lifetime, $N_f = 10,056$ cycles, of all samples in test series 11.

Figure 12b compares predicted fatigue lives until short crack initiation, Equation (4), with the corresponding experimental results. On average, most data points in the diagram are allocated around the 1:1 line, thus suggesting that the fracture mechanics model reasonably predicts short crack initiation. A large scatter of the results can be explained by numerous uncertainties in the input data and underlying assumptions, e.g., material properties and inaccuracies of their approximation (Figure 10), initial crack size and crack initiation site selected to be fixed for all specimens, deterministic approach adopted in this study. Additional uncertainties may arise due to the limited capabilities of the detection of short cracks during the tests. For the sharply notched specimens, no uncertainties should result from defects or material flaws due to the manufacturing process, since geometrically well-defined artificial notches were included. Only for the unnotched specimens could flaws in the material have had an impact. Some of the uncertainties mentioned above are eliminated after a long crack has been initiated. This is demonstrated in Figure 12c, which shows a good agreement between fatigue lives predicted until long crack initiation, Equation (5), and the related experimental observations.

A more detailed view of the results can be gained by plotting them in an S–N diagram for each individual test series, Figure 13. For test series 18, where specimens have a sharp notch ($r = 0.05$ mm, $\omega = 15°$), a good correlation between the number of cycles calculated by fracture mechanics (solid black line) and the total fatigue life (red symbols) can be observed. Accordingly, the lifetime is slightly underestimated by a factor of 2. The ratio between the cycles until long crack initiation and fracture is comparable to the fatigue tests and calculations. The respective ratio corresponds to the difference between the orange and red symbols, on the one hand, and between the grey and black lines, on the other hand. However, the number of cycles to crack initiation $N_{sci,pre}$, estimated by subtracting the total cycles calculated for crack growth from the experimentally determined cycles to fracture, appears to be considerably overestimated as compared to the experimental results. This

result for the sharply notched specimens, Figure 12a, is mainly explained by a small fraction of the $N_{sci,exp}$ cycles in the total fatigue life, $N_{f,exp}$, which constitutes 2–12%. Consequently, any inaccuracy relating to the fracture mechanics model may have a large impact on the estimated number of cycles $N_{sci,pre}$. In contrast, a rather good correlation between experimentally determined and numerically calculated crack initiation cycles is obtained for test series 21 involving specimens with a comparatively mild notch ($r = 0.5$ mm, $\omega = 135°$), especially those tested in the HCF regime. A larger deviation between $N_{sci,pre}$ and $N_{sci,exp}$ at higher stress amplitudes is probably caused by overestimating crack growth rates.

5.3. Statistical Assessment of Influencing Factors

The parameters of the S–N curve were derived from a statistical evaluation using the maximum likelihood method; however, from this evaluation, no measure of the accuracy can be deduced. To test the reliability of the results of the statistical evaluation, a bootstrapping approach was used. For each test series, 1000 resamples with replacements were evaluated. Each resample had the same number of cycles as the original test series and was again analyzed statistically by maximum likelihood. To avoid unrealistically steep slopes of the S–N curves, the minimum slope was set to $k_{min} = 1$. As a result, 1000 S–N curves were derived for one test series with identified individual values of $\Delta\sigma_k$, N_k and k. The variation of the S–N curve parameters and subsequently the accuracy of these values can be visualized in distribution plots, Figure 14.

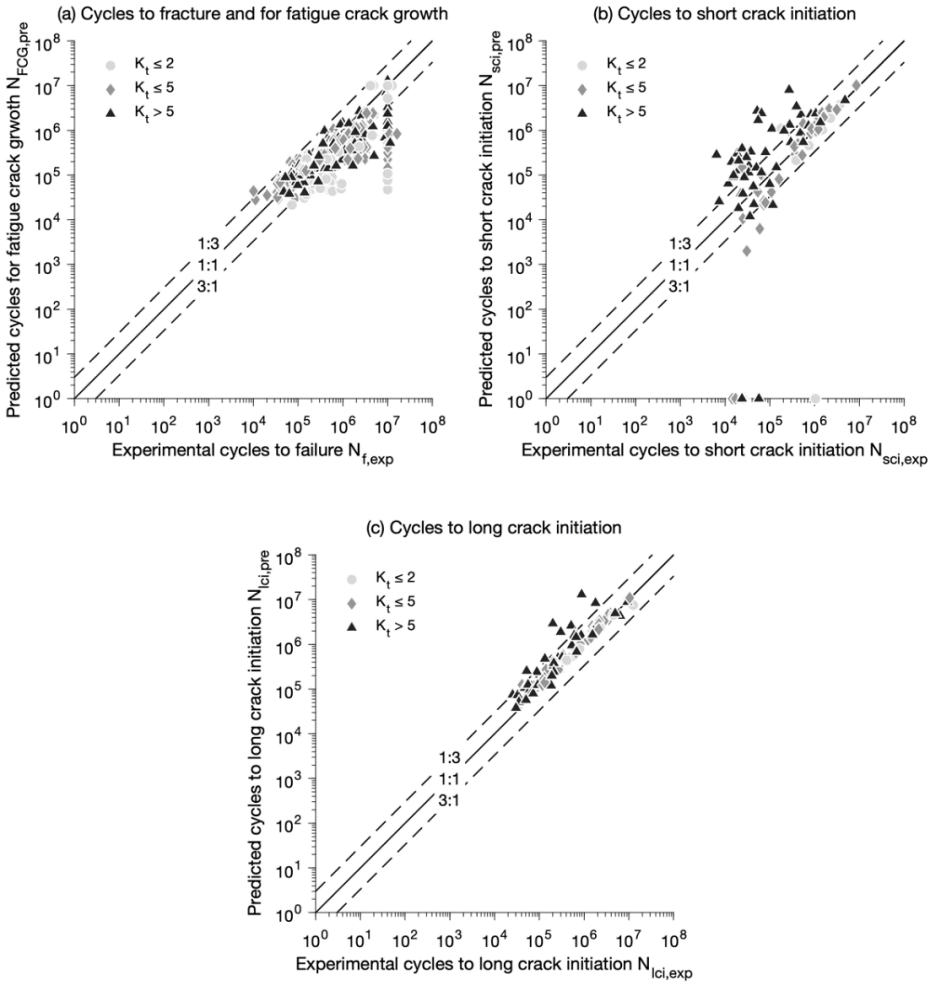

Figure 12. Comparison of (**a**) cycles to fracture and cycles for fatigue crack growth, (**b**) cycles to crack initiation, and (**c**) cycles to long crack initiation.

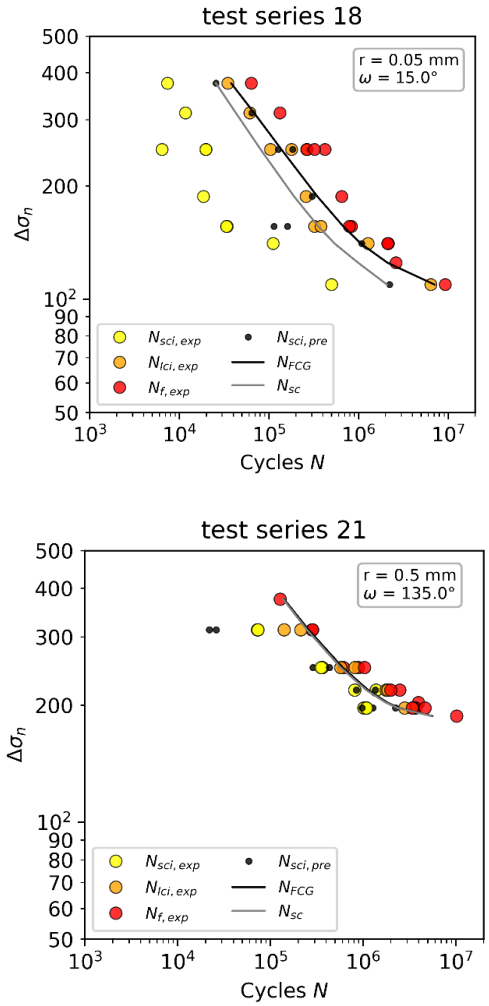

Figure 13. Comparison of S–N data: experimentally derived for three failure criteria, numerically calculated cycles for short crack growth and total crack growth, and derived crack initiation cycles. Material QStE380TM BM.

The width of the filled areas in Figure 14 represents the distribution of the parameters k, N_k and $\Delta\sigma_{n,a,k}$. A small variation of the parameters is indicated if the distribution has a small height, such as that shown for slope k of test series 1. A high variation, as identified, for example, for the slope of test series 2, stands for a high scatter in the S–N data. It indicates that the determined (mean) values might not represent the real parameters. In addition, the derived mean values are plotted with a white dot. The parameters in a range between the 1st and 3rd quartile can be identified by the black line. Next to the distribution of the S–N parameters, their coefficient of variation (CV) is also plotted showing a standardized measure of the dispersion of the probability distribution.

As can be seen, some test series show quite a low scatter in all parameters k, N_k and $\sigma_{n,a,k}$, such as 1, 4, or 20. For some other test series, such as 2, 16, or 26–27, quite a high scatter can be identified. This can directly be attributed to a comparatively high scatter in the original S–N data and a small number of overall tests. Even if the values of the slope and the knee point show high variations, the variation of the endurable stresses at the knee point is comparatively low. It is important to mention that the distributions determined by bootstrapping should be interpreted with care since they are based only on a few data points, the available S–N data; however, the distributions give a good understanding of the reliability of the determined parameters.

In a subsequent step, a correlation analysis between

- shape parameters of the S–N curve k and N_k,

- geometric properties of the specimens r and ω and
- stress concentration factor K_t

was performed. For this, the average values of the slope and the knee point of all 1000 resamples, k_{mean} and N_{mean}, as well as their standard deviation, k_{std} and N_{std}, were calculated.

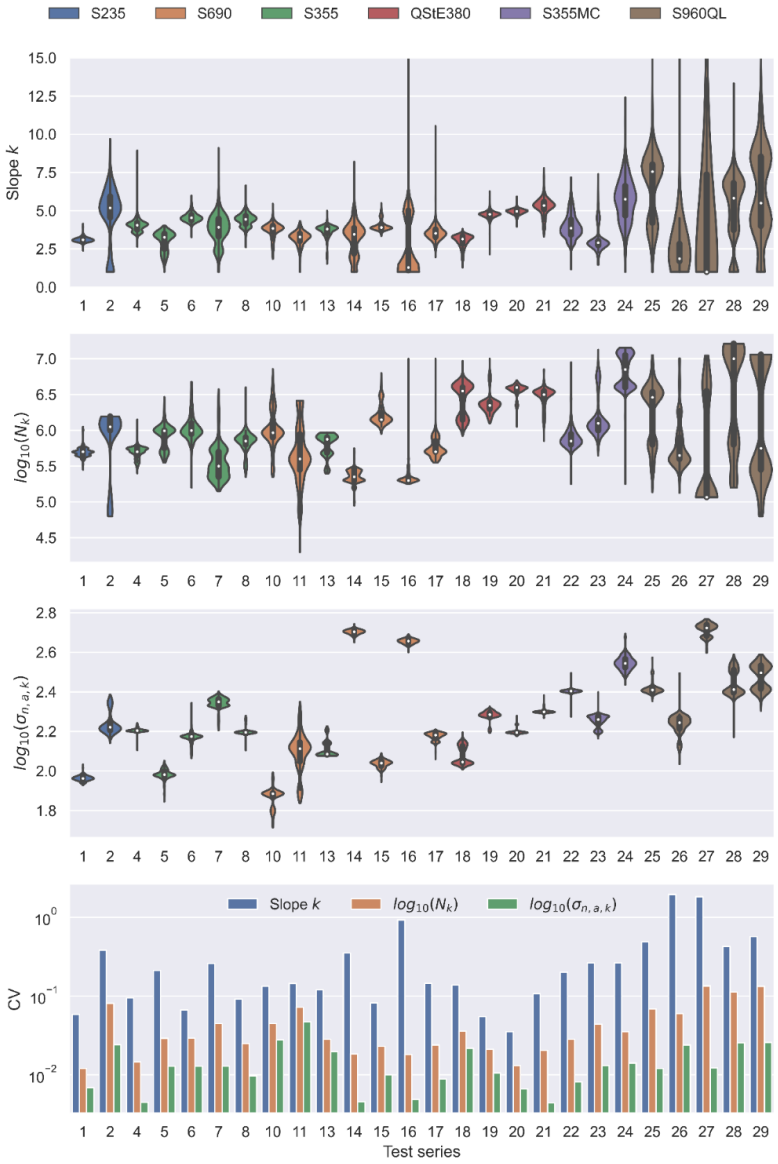

Figure 14. Evaluation of the slope k, location of N_k, $\sigma_{n,k,a}$ and the coefficient of variation (CV) of all test series determined by bootstrapping (minimum slope was set to $k_{min} = 1$).

Again, two different types of correlation coefficients, Pearson's and Spearman's, are determined to assess the statistical interference between the parameters of the S–N curve derived by the maximum likelihood method and other influencing factors (geometrical parameters and hardness). The first one is the Pearson correlation coefficient and the second is Spearman's rank correlation, which is capable of assessing non-linear relations. This is an important aspect, as some parameters are typically expected to have a non-linear impact, e.g., the notch radius on the stress concentration factor. As mentioned before, a correlation above $|r_{xy}| = 0.7$ is often associated with a strong correlation and values below $|r_{xy}| = 0.3$ are typically considered weak.

The results for both types of correlation coefficients are presented in Figure 15 as correlation matrices. Therein, the magnitude of the correlation is displayed by its color

intensity. In other words, darker colors on both sides of the contrasting spectrum are associated with stronger correlations.

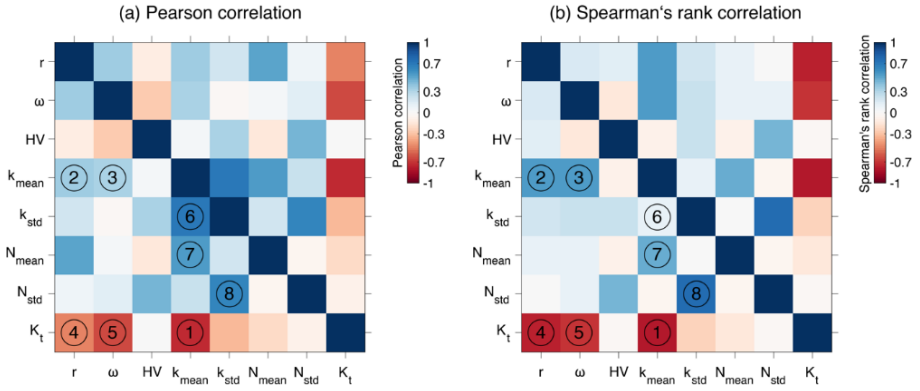

Figure 15. Correlation between maximum likelihood parameters and influencing factors based on (**a**) Pearson (linear) and (**b**) Spearman's (non-linear) rank correlation coefficient.

The main findings from the assessment of correlation coefficients are as follows:

- The highest correlation (marked by "1" in Figure 15) between two variables is observed between the stress concentration factors and the mean slope exponents determined by bootstrapping ($|r_{Pearson}| = 0.72$ and $|r_{Spearman}| = 0.79$). In addition, moderate correlations are determined between the mean slope exponents and the notch radius ($|r_{Pearson}| = 0.37$ and $|r_{Spearman}| = 0.55$), as well as an opening angle ($|r_{Pearson}| = 0.33$ and $|r_{Spearman}| = 0.56$), marked by "2" and "3", respectively.
- Unsurprisingly, moderate to strong correlations are also observed for the relation between stress concentration factors, and either the notch radius ($|r_{Pearson}| = 0.48$ and $|r_{Spearman}| = 0.77$) or the opening angle ($|r_{Pearson}| = 0.65$ and $|r_{Spearman}| = 0.71$), marked by "4" and "5", respectively.
- The reason for the higher Spearman-type correlations for the aforementioned parameters is expected to be related to their non-linear interaction, which is expected to be better assessed using a non-linear type of correlation coefficient.
- While there is a Pearson correlation (marked by "6") between the mean and scatter of the slope exponents ($|r_{Pearson}| = 0.7$), there is no such correlation according to Spearman's rank correlation. Assessing the results, it is found that the strong Pearson correlation is related to one outlier. This supports the assumption that a Pearson correlation coefficient is more prone to outliers.
- Additionally, a moderate correlation is observed between the means of the knee points and the means of the slope exponents ($|r_{Pearson}| = 0.54$ and $|r_{Spearman}| = 0.49$) and a fairly strong correlation between the standard deviations of both variables ($|r_{Pearson}| = 0.65$ and $|r_{Spearman}| = 0.76$), marked by "7" and "8", respectively. The second correlation is thought to be systematically related to the general increase in scattering in the fatigue test results with decreasing notch acuity.

In addition to the correlation matrixes, a symbolic regression was conducted with the same input data using the Python toolkit *sklearn*. As identified in the correlation matrices, the slope k has a strong correlation to K_t and can be expressed by Equation (7). The slope gets steeper with increasing stress concentration.

$$k = 6.6 - \sqrt{K_t} \tag{9}$$

In contrast, no meaningful and interpretable correlation between the position of the knee point and the geometric and material parameters of the specimens could be achieved. This result is also in line with the correlation matrices, in Figure 15.

6. Discussion

A large number of artificially notched specimens differing with respect to the notch acuity, material strength, and microstructural properties, were tested until fracture, leading to different fatigue characteristics. Overall, 26 test series, including 351 specimens, were considered in the analysis. For each test series, the material was characterized (geometry, misalignment, and hardness measured) and the influence of misalignments caused by welding was quantified by means of the strain gauges. As a basis for the fatigue crack growth calculations, a parametric FE model was created and used to determine the actual stress profiles along the expected crack path for each specimen. Thereby, it was possible to model the specimens in the most accurate way, including misalignment-induced secondary bending stresses.

For the majority of specimens, crack initiation was detected visually or per gauges showing a dependency of crack initiation duration on the notch acuity. Principally, fatigue cracks initiated early in the case of crack-like notches, whereas the fraction of load cycles before crack initiation increased with decreasing notch stress range, as indicated in Figure 11b.

The statistical evaluation of the S–N curves with the maximum likelihood approach proved to be a good method to provide information on the S–N curve, i.e., its parameters knee point N_k, slope k and the endurable stress at the knee point $\sigma_{n,a,k}$; however, the determined position of N_k at the location of the smallest value of the support function is accompanied by uncertainties, especially in cases where the support function does not have a pronounced minimum, see Figure 7, bottom right.

A measure of the accuracy of the values can be derived by bootstrapping the S–N data. With this approach, a standard deviation as a measure of the accuracy can be assigned to each value. It must be mentioned that the bootstrapping might lead, in some cases, to unrealistic results that increase in number with the scatter of the S–N curve and the number of resamples. Therefore, extreme values, as can be identified in Figure 14 by a small distribution width, should not be over-interpreted.

The coefficients of variation of the three parameters k, N_k, and $\sigma_{a,n,k}$ from bootstrapping show clearly that the values of the slope k have the highest variation, followed by the ones of the knee point N_k; however, it was observed that the value ranges are not directly comparable. A change in slope from, e.g., 5 to 6 is, in terms of the endurable number of cycles, small compared to a change of the knee point from $log10(N_k) = 5$ to 6, i.e., from 10^5 to 10^6.

The results in Section 5.1 suggest that the total fatigue life of notched specimens can rather accurately be predicted by a fracture mechanics approach; however, this requires comprehensive material data, including FCG curves and tensile properties for different weld zones, including the base metal and HAZ. As such data are rarely available, they can be estimated. In this study, only two experimental datasets on FCG curves were involved—for S355NL and S960QL steel grades, both related to the base metal. Subsequently, those FCG curves were used for other materials with similar strength properties and for other microstructural zones of the same steel grade. Another problem faced in the strength assessment of welded components is missing information on the local strength properties of the weld metal and HAZ. As a pragmatic solution, both the yield strength and the tensile strength were estimated in all cases, including the base metal, from the hardness measurements. Finally, a unique definition of an initial surface crack, referred to as a short crack, was employed in all fracture mechanics calculations. Accordingly, an assumption of a semi-elliptical crack with the depth of $a_{sci} = 0.5$ mm and the length of $2c_{sci} = 1$ mm was found to yield an optimal accuracy in predicting fatigue lives of all test series. An essential feature of sharply notched specimens is a high-stress level at the notch root and, consequently, plastic deformations achieved for a considerable number of specimens analyzed. These effects were accounted for by means of a proper plasticity correction applied to the stress intensity factors.

The predicted fatigue lives associated with crack propagation, $N_{FCG,pre}$, are in good agreement with the total fatigue lives, $N_{f,exp}$, determined in the tests. For 77% of all

specimens, the fracture mechanics approach yields $N_{FCG,pre} < N_{f,exp}$ (see Figure 12) and, thus, allow for estimating the number of cycles until crack initiation. In the other cases, the fracture mechanics model results in a non-conservative lifetime prediction and, thus, in negative estimates of the lifetime until crack initiation, $N_{sci,pre}$. The latter conclusion holds for some of the specimens of the following six test series:

- Series 13: material S355J2+N, base metal, notch opening angle $\omega = 0°$
- Series 5 and 6: material S355J2+N, HAZ, notch opening angle $\omega = 0°$ and $\omega = 135°$, respectively.
- Series 10 and 11: material S690QL, HAZ, notch opening angle $\omega = 0°$ and $\omega = 135°$, respectively.
- Series 24: material S355MC, HAZ, unnotched specimens, $\omega = 180°$

For test series 13, $N_{FCG,pre}$ and $N_{f,exp}$ are in good agreement: all points are bounded by the 1:3 and 3:1 lines, and an approximately equal number of points are located above and below the 1:1 line. Hence, non-conservative lifetime prediction in this test series is mainly attributed to the experimental data scatter and the fact that the sharp notch leads to very early crack initiation. For the other five test series, all with the crack position in the HAZ, the main reason for the non-conservative prediction is likely due to an inaccurate estimation of the respective FCG curves. For better confidence in a fracture mechanics model, additional FCG tests are required on specimens extracted from the HAZ with different microstructure and strength properties.

In addition, multiple crack initiation was observed during fatigue testing for some specimens. These cracks coalesced in the following cycles and formed a longer crack. Similarly, some cracks did not initiate in the middle of the notch but closer to one of the edges. For such scenarios, deviations in prediction accuracy are inevitable. This also influences the crack propagation behavior and therefore leads to lower prediction accuracy.

Based on the statistical evaluation, it was possible to determine correlations between influencing factors and the shape of the S–N curves. Two different correlation coefficient types, linear Pearson and non-linear Spearman rank, were used, as it is known that some factors follow a non-linear relation. The highest correlation between two variables is observed between the stress concentration factor and the mean slope exponents determined by bootstrapping. In addition, moderate Spearman rank correlations are also determined between the mean slope exponent and the notch geometry, represented by the notch radius as well as the opening angle. Interestingly, there seems to be no effect on the mean and standard deviation of the bootstrapped knee point of the S–N curves. This is in contrast to former studies, e.g., by Hück et al. [51], who determined a logarithmic relation between the stress concentration factor and both the slope k and the knee point N_k of the S–N curves for base materials. The results presented in the current study do not agree with the concept of normalized S–N scatter bands by Haibach [25]. He argued that differences in the slopes of the S–N curves are related to the fact that for lower notch acuity, a large part of fatigue tests performed at high-stress ranges fall into the transition region from the high-cycle to the low-cycle fatigue regime. For plain specimens ($K_t \approx 1$), this effect is even more pronounced due to gross cyclic plastification at high-stress ratios (corresponding to a small number of cycles to failure, $N_f < 10^5$ cycles). As a considerable amount of test data for this study is based on a test of high strength steels with the number of cycles to failure above 10^5 cycles, there is clear evidence that there is a relation between the slope of S–N curves and the notch acuity. In fact, this agrees with one conclusion presented by Hück et al. [51].

As mentioned in Section 2, the slope of welded joints is set to $k = 3$ in most rules and recommendations. This assumption is in contradiction to the relationship identified in this work. Only BS 7608 [21] recommends a slightly shallower slope for weld details with low-stress concentration factors; however, it should be noted, that the specimens considered here have only three weld characteristics, (i) sharp notches, (ii) typical notch opening angles, and (iii) typical microstructural properties in the area of crack initiation and crack propagation. Other characteristics that may have an influence on the course of the S–N curves, such as residual stresses, a varying weld profile, or inner weld imperfections,

are not considered. It can be assumed that the quality of the butt joints that build the experimental basis for the recommendation in rules and guidelines was not high, and the joints contained strong irregularities and, consequently, stress raisers.

In this investigation, no correlation between geometrical or metallurgical features and the knee point was identified. This stands in contrast to some guidelines that correlate the knee point to the weld details but likely explains the circumstance that there is no common agreement between all major guidelines. As for the knee point, it has to be mentioned that the specimens investigated in this work show only some features of welded joints. A further re-analysis of (high-quality) fatigue data for welded joints needs to be performed in which all relevant properties are well documented.

7. Conclusions

This study investigated the relationship between fatigue crack initiation and propagation in welded joints using artificially notched specimens with welded joint characteristics of different notch acuity (different radii and opening angles). From the statistical and numerical assessment of the experiments, the following conclusions are obtained:

- The fracture mechanics approach allows for a reasonable prediction of the total fatigue life. In most cases, 77% of the specimens analyzed, this approach leads to conservative estimates of fatigue lives. For the rest of the 23% of the specimens, the fatigue life is overestimated by a maximum factor of 3. The assumption of an initial semi-elliptical crack with the depth of $a_{sci} = 0.5$ mm and the length of $2c_{sci} = 1$ mm appeared to be a good compromise for all 26 test series. In the fracture mechanics calculations, plasticity deformations at the notch root need to be taken into account. This was achieved in this study by applying a plasticity correction to the stress intensity factors, based on the FAD approach. Non-conservative results and relatively large data scatter observed for some of the test series are believed to be partly attributed to assumptions related to fatigue crack growth curves and inaccuracies resulting from their smooth curve fitting. Additional inaccuracies may result from a simplified analysis approach assuming a single crack initiation site in the middle of the specimen thickness, thus ignoring possibilities of multiple crack initiation or crack initiation at the specimen edge. Both latter scenarios would result in a shorter fatigue life as compared to the model adopted in this study.
- For sharply notched specimens, the initiation phase is negligible and the total fatigue life is dominated by fatigue crack propagation. Therefore, the back-calculation of the fatigue crack initiation phase, N_{sci}, is subject to large errors. In contrast, such estimates of N_{sci} are shown to be rather accurate for mild notches.
- The bootstrapping of the S–N data is a suitable statistical method to identify the accuracy of the evaluated S–N parameters and to determine statistically validated estimates for the slope k and the knee point N_k of the S–N curves.
- Depending on the chosen correlation coefficient type, a moderate to almost strong correlation between applied notch stress range $\Delta\sigma_{notch}$ with the ratio between experimental cycles to short $N_{sci,exp}$ or long crack initiation $N_{lci,exp}$. and cycles to fracture $N_{f,exp}$ were determined, Figure 11. In addition, the assessment supports the general understanding that the crack initiation portion dominates in the high-cycle fatigue regime, whereas the crack propagation stage dominates in the medium- and low-cycle fatigue regime, see Radaj et al. [1] and Murakami [5].
- Using artificially notched specimens and statistical methods, it was shown that the slope k but not the knee point N_k. of the S–N curves correlate to the notch acuity, the latter being defined by the notch radius and the notch opening angle, or the stress concentration factor.

Author Contributions: Conceptualization, methodology, validation, formal analysis, and investigation, M.B., J.B., C.F. and I.V.; software, M.B., J.B. and I.V.; data curation, M.B., C.F., J.B., M.H. and I.V.; visualization, M.B. and J.B.; writing—original draft preparation, M.B., C.F., J.B., M.H. and I.V.;

writing—review and editing, M.B., C.F., J.B., M.H. and I.V.; funding acquisition, J.B. and I.V. All authors have read and agreed to the published version of the manuscript.

Funding: The Federal Ministry for Economic Affairs and Energy BMWi funded the work of J.B. and M.H. by the AiF e.V. (Arbeitsgemeinschaft industrieller Forschungsvereinigungen "Otto von Guericke" e.V.) under grant 20.366 BG.

Data Availability Statement: Not applicable.

Acknowledgments: This paper is an extended version of the reference [15] previously published in the conference proceedings of the DVM (German Association for Materials Research and Testing). M.B. would like to thank Franziska Rolof for helping with the specimen's preparation.

Conflicts of Interest: The authors declare no conflict of interest.

Nomenclature

Symbol	Unit	Description
a_{lc}	mm	Depth of a through-thickness (long) crack
a_{sci}	mm	Depth of a semi-elliptical (short) crack
c_{sci}	mm	Half-length of a semi-elliptical (short) crack
C_i	-	Material parameters in crack growth equation
CV	-	Coefficient of variation
d	mm	Notch depth
f	Hz	Test frequency
$f(L_r)$	-	Plasticity correction factor
$f(R_n)$	-	Nominal stress ratio correction factor
HV	-	Vickers hardness
k	-	Slope of the S–N curve at $N < N_k$
k^*	-	Slope of the S–N curve at $N > N_k$
k_{mean}, k_{std}	-	Mean and standard deviation of the slope of the S–N curve in the high cycle fatigue regime ($N \leq N_k$) obtained from bootstrapping
$K_{I,max}$, $K_{J,min}$, ΔK_J	MPa$\sqrt{m}$	Maximum and minimum stress intensity factor, and stress intensity factor range including plasticity correction
K_{max}, K_{min}, ΔK	MPa$\sqrt{m}$	Maximum and minimum stress intensity factor, and stress intensity factor range
K_t	-	Stress concentration factor
L_r, ΔL_r	-	Plasticity parameter and its range
N_{FCG}	Cycle	Cycles spend in crack propagation
N_G	Cycle	Maximum number of cycles for which a test is considered a runout
N_f, $N_{f,exp}$	Cycle	Cycles to fracture and experimental cycles to fracture
N_{sci}, $N_{sci,exp}$, $N_{sci,pre}$	Cycle	Cycles to short crack initiation, respective experimental and predicted values
N_{lci}, $N_{lci,exp}$, $N_{lci,pre}$	Cycle	Cycles to long crack initiation, respective experimental and predicted values
N_k	Cycle	Cycles at the knee point
P	-	Probability of survival
r	mm	Radius of notch
R	-	Nominal stress ratio
R_K, R_{K_J}	-	Stress intensity ratio related to ΔK and ΔK_J
R_m, $R_{p0.2}$	MPa	Material ultimate strength and yield strength
R_{notch}	mm	Stress ratio of local stresses
r_{xy}, $r_{Pearson}$, $r_{Spearman}$	-	Correlation coefficient, Pearson's correlation coefficient, and Spearman's rank correlation coefficient
t	mm	Specimen thickness
T_S	-	Scatter ratio in stress direction
x	mm	Distance from the notch root in crack growth direction
w	mm	Specimen width

ΔK_{th}	MPa$\sqrt{m}$	Threshold of the crack intensity factor range
$\Delta\sigma_{n,k}$	MPa	Nominal stress range at the knee point
$\Delta\sigma_{nom}$	MPa	Nominal stress range
$\Delta\sigma_{notch}$	MPa	Stress range at the notch
σ_1	MPa	Maximum principal stress
ω	°	Notch opening angle

Abbreviations

BM	Base material
HAZ	Heat affected zone
WM	Weld metal

Appendix A

Table A1. Results of the statistical evaluation of the S–N curves with maximum likelihood.

Test Series	Slope k	Stress S_k	Knee Point N_k [$\times 10^3$]	Scatter 1:T_S	Slope k	Stress S_k	Knee Point N_k [$\times 10^3$]	Scatter 1:T_S
	Maximum Likelihood Evaluation with Original Data				Maximum Likelihood Evaluation from Bootstrapping (Mean Values)			
1	3.11	91.7	501	1.11	3.12	92.0	504	1.10
2	5.32	165.2	1122	1.36	4.79	175.3	1032	1.30
4	4.03	160.9	501	1.06	4.03	161.0	503	1.05
5	3.29	93.3	1000	1.23	3.02	96.5	875	1.18
6	4.54	149.0	1000	1.14	4.57	147.5	1197	1.12
7	3.91	227.1	316	1.18	3.80	221.4	445	1.16
8	4.54	155.7	794	1.08	4.41	159.4	720	1.06
10	3.79	77.1	891	1.16	3.74	74.2	1267	1.14
11	3.28	130.3	398	1.35	3.22	127.4	716	1.31
13	3.78	121.7	794	1.08	3.67	129.8	664	1.06
14	3.49	502.7	251	1.24	3.15	505.3	233	1.22
15	3.83	110.3	1413	1.10	4.02	109.0	1753	1.09
16	1.14	454.9	200	1.23	2.48	453.5	233	1.20
17	3.43	153.1	501	1.13	3.55	150.3	611	1.11
18	3.24	109.7	3981	1.22	3.02	120.7	2985	1.18
19	4.78	193.2	2239	1.09	4.75	192.0	2429	1.08
20	4.99	155.7	3981	1.05	4.95	158.0	3704	1.05
21	5.33	199.6	3162	1.08	5.28	200.1	3120	1.07
22	3.80	254.3	708	1.10	4.00	251.9	891	1.07
23	2.94	181.5	1259	1.14	3.12	179.1	1909	1.11
24	5.79	339.6	8913	1.34	5.74	352.8	7816	1.27
25	7.98	249.0	3981	1.15	6.71	261.6	2646	1.11
26	1.74	179.7	398	1.21	3.16	173.4	1025	1.16
27	5.00	548.8	116	1.29	8.05	520.7	1883	1.16
28	6.37	251.3	10,000	1.41	5.15	284.3	7385	1.31
29	3.92	332.6	282	1.36	6.18	302.9	4879	1.25

References

1. Radaj, D.; Sonsino, C.M.; Fricke, W. *Fatigue Assessment of Welded Joints by Local Approaches*, 2nd ed.; Woodhead Publishing: Cambridge, UK, 2006.
2. Zerbst, U.; Madia, M.; Schork, B.; Hensel, J.; Kucharczyk, P.; Ngoula, D.; Tchuindjang, D.; Bernhard, J.; Beckmann, C. *Fatigue and Fracture of Weldments*; Springer: Berlin/Heidelberg, Germany, 2019. [CrossRef]
3. Baumgartner, J.; Waterkotte, R. Crack initiation and propagation analysis at welds—Assessing the total fatigue life of complex structures. *Mater. Werkst.* **2015**, *46*, 123–135. [CrossRef]
4. Fischer, C.; Fricke, W. Effect of the stress distribution in simple welded specimens and complex components on the crack propagation life. *Int. J. Fatigue* **2016**, *92*, 488–498. [CrossRef]
5. Murakami, Y. *Metal Fatigue: Effects of Small Defects and Nonmetallic Inclusions*, 2nd ed.; Academic Press: Cambridge, MA, USA, 2019. [CrossRef]
6. Mann, T.; Tveiten, B.W.; Härkegård, G. Fatigue crack growth analysis of welded aluminium RHS T-joints with manipulated residual stress level. *Fatigue Fract. Eng. Mater. Struct.* **2006**, *29*, 113–122. [CrossRef]
7. Remes, H. *Strain-Based Approach to Fatigue Strength Assessment of Laser-Welded Joints*; Helsinki Univercity of Technolgy: Espoo, Finland, 2008.
8. Song, W.; Liu, X.; Xu, J.; Fan, Y.; Shi, D.; He, M.; Wang, X.; Berto, F. Fatigue fracture assessment of 10CrNi3MoV welded load-carrying cruciform joints considering mismatch effect. *Fatigue Fract. Eng. Mater. Struct.* **2021**, *44*, 1739–1759. [CrossRef]
9. Toyosada, M.; Gotoh, K.; Niwa, T. Fatigue life assessment for welded structures without initial defects: An algorithm for predicting fatigue crack growth from a sound site. *Int. J. Fatigue* **2004**, *26*, 993–1002. [CrossRef]
10. Fricke, W.; Gao, L.Y.; Paetzold, H. Fatigue assessment of local stresses at fillet welds around plate corner. *Int. J. Fatigue* **2017**, *101*, 169–176. [CrossRef]
11. Barsoum, Z.; Jonsson, B. Fatigue Assessment and LEFM Analysis of Cruciform Joints Fabricated with Different Welding Processes. *Weld. World* **2008**, *52*, 93–105. [CrossRef]
12. Chapetti, M.D.; Steimbreger, C. A simple fracture mechanics estimation of the fatigue endurance of welded joints. *Int. J. Fatigue* **2019**, *125*, 23–34. [CrossRef]
13. Zong, L.; Shi, G.; Wang, Y.-Q.; Li, Z.-X.; Ding, Y. Experimental and numerical investigation on fatigue performance of non-load-carrying fillet welded joints. *J. Constr. Steel Res.* **2017**, *130*, 193–201. [CrossRef]
14. Liu, Y.; Tsang, K.S.; Hoh, H.J.; Shi, X.; Pang, J.H.L. Structural fatigue investigation of transverse surface crack growth in rail steels and thermite welds subjected to in-plane and out-of-plane loading. *Eng. Struct.* **2020**, *204*, 110076. [CrossRef]
15. Braun, M.; Fischer, C.; Baumgartner, J.; Hecht, M.; Varfolomeev, I. Zum Verhältnis von Rissinitiierung und -ausbreitung an gekerbten Proben mit Schweißnahtcharakteristik. In Proceedings of the 54. Tagung Bruchmechanische Werkstoff und Bauteilbewertung: Beanspruchungsanalyse, Prüfmethoden und Anwendungen, Berlin, Germany, 23 February 2022.
16. Hobbacher, A.F. *Recommendations for Fatigue Design of Welded Joints and Components*, 2nd ed.; Springer International Publishing: Cham, Switzerland, 2016. [CrossRef]
17. DNV GL AS. *DNVGL-RP-C203: Recommended Practice for Fatigue Design of Offshore Steel Structures*; DNV GL AS: Høvik, Norway, 2016.
18. *EN 1993-1-9:2005*; Eurocode 3: Design of Steel Structures—Part 1–9: Fatigue. European Committee for Standardization: Brussels, Belgium, 2005.
19. Forschungskuratorium Maschinenbau (FKM). *Analytical Strength Assessment of Components: FKM Guideline*, 6th ed.; VDMA: Frankfurt, Germany, 2012.
20. Baumgartner, J. Review and considerations on the fatigue assessment of welded joints using reference radii. *Int. J. Fatigue* **2017**, *101*, 459–468. [CrossRef]
21. *BS 7608:2014+A1:2015*; Guide to Fatigue Design and Assessment of Steel Products. British Standards Institution BSI: London, UK, 2014.
22. American Welding Society. *AWS D1.1:2010 Structural Welding Code—Steel*; American Welding Society: Miami, FL, USA, 2010.
23. Japanse Society of Steel Construction. *Fatigue Design Recommendations for Steel Structures*; Japanese Society of Steel Construction: Tokyo, Japan, 1995.
24. Renken, F.; von Bock und Polach, R.U.F.; Schubnell, J.; Jung, M.; Oswald, M.; Rother, K.; Ehlers, S.; Braun, M. An algorithm for statistical evaluation of weld toe geometries using laser triangulation. *Int. J. Fatigue* **2021**, *149*, 106293. [CrossRef]
25. Haibach, E. *Betriebsfestigkeit: Verfahren und Daten zur Bauteilauslegung*, 3rd ed.; Springer: Berlin/Heidelberg, Germany; New York, NY, USA, 2006.
26. Socie, D.F.; Marquis, G.B. *Multiaxial Fatigue*; SAE International: Warrendale, PA, USA, 1999.
27. Fiedler, M.; Wächter, M.; Varfolomeev, I.; Vormwald, M.; Esderts, A. *Rechnerischer Festigkeitsnachweis unter Expliziter Erfassung Nichtlinearen Werkstoffverformungsverhaltens für Bauteile aus Stahl, Stahlguss und Aluminiumknetlegierungen*; VDMA Verlag: Frankfurt, Germany, 2019.
28. *BS 7910:2019*; Guide to Methods for Assessing the Acceptability of Flaws in Metallic Structures. British Standards Institution: London, UK, 2019.
29. Bowness, D.; Lee, M.M.K. *Fracture Mechanics Assessment of Fatigue Cracks in Offshore Tubular Structures*; Offshore Technology Report 2000/077; Health and Safety Executive: Bootle, UK, 2002.
30. Forman, R.; Shivakumar, V.; Mettu, S.; Newman, J. Fatigue crack growth computer program NASGRO version 3.0. In *Reference Manual, NASA JSC-22267B*; NASA: Washington, DC, USA, 2000.

31. Paris, P.C.; Bucci, R.J.; Wessel, E.T.; Clark, W.G.; Mager, T.R. Extensive Study of Low Fatigue Crack Growth Rates in A533 and A508 Steels. In *Stress Analysis and Growth of Cracks. Proceedings of the 1971 National Symposium on Fracture Mechanics: Part 1*; ASTM International: West Conshohocken, PA, USA, 1972; Volume 513, pp. 141–176. [CrossRef]
32. Dowling, N.; Begley, J. Fatigue crack growth during gross plasticity and the J-integral. In *Mechanics of Crack Growth*; ASTM International: West Conshohocken, PA, USA, 1976.
33. Wüthrich, C. The extension of the J-integral concept to fatigue cracks. *Int. J. Fract.* **1982**, *20*, R35–R37. [CrossRef]
34. McClung, R.C.; Chell, G.G.; Lee, Y.D.; Russel, D.A.; Orient, G.E. *Development of a Practical Methodology for Elastic-Plastic and Fully Plastic Fatigue Crack Growth*; ASTM International: West Conshohocken, PA, USA; Marshall Space Flight Center: Huntsville, AL, USA, 1999.
35. Zerbst, U.; Madia, M.; Hellmann, D. An analytical fracture mechanics model for estimation of S–N curves of metallic alloys containing large second phase particles. *Eng. Fract. Mech.* **2012**, *82*, 115–134. [CrossRef]
36. British Energy Generation Limited. *R6, Assessment of the Integrity of Structures Containing Defects, Revision 4*; British Energy Generation Limited: London, UK, 2001.
37. Fischer, C.; Fricke, W.; Rizzo, C.M. Fatigue tests of notched specimens made from butt joints at steel. *Fatigue Fract. Eng. Mater. Struct.* **2016**, *39*, 1526–1541. [CrossRef]
38. Baumgartner, J. *Schwingfestigkeit von Schweißverbindungen unter Berücksichtigung von Schweißeigenspannungen und Größeneinflüssen*; Fraunhofer Verlag: Stuttgart, Germany, 2014.
39. *ISO 6507-1:2005*; Metallic Materials—Vickers Hardness Test—Part 1: Test Method. International Standards Organization: Geneva, Switzerland, 2005.
40. Störzel, K.; Baumgartner, J. Statistical evaluation of fatigue tests using maximum likelihood. *Mater. Test.* **2021**, *63*, 714–720. [CrossRef]
41. Sonsino, C. Course of SN-curves especially in the high-cycle fatigue regime with regard to component design and safety. *Int. J. Fatigue* **2007**, *29*, 2246–2258. [CrossRef]
42. Spindel, J.E.; Haibach, E. The method of maximum likelihood applied to the statistical analysis of fatigue data. *Int. J. Fatigue* **1979**, *1*, 81–88. [CrossRef]
43. Braun, M.; Müller, A.M.; Milaković, A.-S.; Fricke, W.; Ehlers, S. Requirements for stress gradient-based fatigue assessment of notched structures according to theory of critical distance. *Fatigue Fract. Eng. Mater. Struct.* **2020**, *43*, 1541–1554. [CrossRef]
44. Zerbst, U. *Analytische bruchmechanische Ermittlung der Schwingfestigkeit von Schweißverbindungen (IBESS-A3)*; Bundesanstalt für Materialforschung und-Prüfung (BAM): Berlin, Germany, 2016.
45. Wang, X.; Lambert, S.B. Stress intensity factors for low aspect ratio semi-elliptical surface cracks in finite-thickness plates subjected to nonuniform stresses. *Eng. Fract. Mech.* **1995**, *51*, 517–532. [CrossRef]
46. Sattari-Far, I.; Dillström, P. Local limit load solutions for surface cracks in plates and cylinders using finite element analysis. *Int. J. Press. Vessel. Pip.* **2004**, *81*, 57–66. [CrossRef]
47. Fett, T.; Munz, D. *Stress Intensity Factors and Weight Functions for One-Dimensional Cracks*; Kernforschungszentrum Karlsruhe: Karlsruhe, Germany, 1994.
48. Willoughby, A.A.; Davey, T.G. Plastic Collapse in Part-Wall Flaws in Plates. In *Fracture Mechanics: Perspectives and Directions (Twentieth Symposium)*; Wei, R.P., Gangloff, R.P., Eds.; ASTM International: West Conshohocken, PA, USA, 1989; Volume ASTM. [CrossRef]
49. Pavlina, E.J.; Van Tyne, C.J. Correlation of Yield Strength and Tensile Strength with Hardness for Steels. *J. Mater. Eng. Perform.* **2008**, *17*, 888–893. [CrossRef]
50. Caruso, J.C.; Cliff, N. Empirical Size, Coverage, and Power of Confidence Intervals for Spearman's Rho. *Educ. Psychol. Meas.* **1997**, *57*, 637–654. [CrossRef]
51. Hück, M.; Thrainer, L.; Schütz, W. *Berechnung von Wöhlerlinien für Bauteile aus Stahl, Stahlguß und Grauguß: Synthetische Wöhlerlinien*, 3rd ed.; Stahleisen: Düsseldorf, Germany, 1983.